J Solid State Electrochem (2005) 9: 138–145
DOI 10.1007/s10008-004-0564-3

ORIGINAL PAPER

**Adel Attia · Markéta Zukalová · Jiří Rathouský**
**Arnošt Zukal · Ladislav Kavan**

# Mesoporous electrode material from alumina-stabilized anatase $TiO_2$ for lithium ion batteries

Received: 26 January 2004 / Accepted: 26 April 2004 / Published online: 16 July 2004


**Abstract** A mesoporous electrode material whose structure is composed of anatase nanocrystals stabilized by alumina is reported. Powder X-ray diffraction shows the anatase phase only, but micro-Raman spectroscopy shows that the materials have a core-shell morphology with grains of bulk anatase covered by a thin rutile layer on the surface. This structure is unique when compared to analogous materials stabilized by zirconia (PNNL-1). Nitrogen adsorption isotherms demonstrate a monotonous increase in surface area and mesopore volume with increasing Al content. Thin film electrodes from these materials were characterized by lithium insertion electrochemistry. Cyclic voltammograms exhibit significant differences in Li accommodation in Al-free and Al-stabilized materials.

**Keywords** Titanium dioxide · Alumina · Lithium battery · Mesoporous materials

## Introduction

The use of nanocrystalline oxide materials in Li-ion batteries results in higher charging rates due to smaller transport distances in the solid host [1]. By decreasing the crystal dimensions, the solid-state $Li^+$ diffusion is progressively replaced by surface-confined Li-storage; in other words there is a natural link between batteries and supercapacitors in the area of nanosized crystals [1]. However, ultrasmall crystals are handicapped by sluggish Li-transport [2, 3, 4] and by charge irreversibility due to parasitic surface reactions [3]. Hence, there is an optimal crystal size for the given host material for fast Li-charging/discharging [3].

Anatase $TiO_2$ electrodes are used in solar cells, lithium batteries and electrochromic devices [5, 6, 7, 8]. Nanocrystalline $TiO_2$(anatase) is a promising electrode material for Li-ion batteries, due to its good Li-storage capacity, cycling-stability and safety against overcharging [9]. Its non-toxicity, environmental compatibility, and low price are other practical advantages of $TiO_2$. However, the performance of nanocrystalline $TiO_2$ for Li-storage is significantly controlled by the particle morphology [7, 8, 10, 11]. For instance, the $TiO_2$ nanosheets clearly exhibit charging in the supercapacitive regime [11], and this effect is also found in mesoporous anatase made by supramolecular templating [10].

The surfactant-templated synthesis of $TiO_2$ mesoporous molecular sieves (analogous to siliceous mesoporous molecular sieves such as MCM-41) was announced in 1995, but this work was later questioned [12]. The synthetic procedures that appeared to be successful for mesoporous silica usually fail for $TiO_2$. The reason is that the original mesoporous $TiO_2$/template composite easily collapses during calcination (detemplating) because of the easy crystallization of titanium dioxide [12, 13]. The only exception to this rule is templating by triblock copolymers, as pioneered by Stucky et al [14, 15, 16], which gives well-organized mesoporous anatase materials upon calcination [10, 14, 15, 16, 17]. An alternative synthetic strategy is based on protecting the surfactant-templated mesoporous $TiO_2$framework by deliberately adding an inorganic component. This synthetic protocol was first demonstrated by Elder et al [18] on zirconia-stabilized $TiO_2$ ($Zr/Ti = 1/3$), called PNNL-1. The material contained anatase crystallites, ~3 nm in size, which were separated by a solid solution of amorphous $Zr_xTi_{1-x}O_4$. It exhibited enhanced thermal stability and interesting electrochemical properties compared to those of ordinary nanocrystalline anatase [7].

A. Attia (✉)
Department of Physical Chemistry,
National Research Centre,
El-Tahrir St., Dokki, 12622 Cairo, Egypt
E-mail: adel_attia@hotmail.com
Fax: +002-02-3370931

A. Attia · M. Zukalová · J. Rathouský · A. Zukal · L. Kavan
J. Heyrovský Institute of Physical Chemistry,
Academy of Sciences of the Czech Republic,
Dolejškova 3, 182 23 Prague 8, Czech Republic

There are various examples of advanced materials based on the titania/alumina system. Alumina coating is widely used for stabilization of $TiO_2$ (rutile)-based white pigments against photodecomposition [19]. Recently, Durrant et al [20] and Fujishima et al [21] reported that a similar alumina coating on $TiO_2$ (anatase) also prevents charge recombination in dye sensitized solar cells, and so leads to significant improvement of the efficiency of solar energy conversion. Aluminum was found to be crucial to the stabilization of the anatase lattice during chemical transport reactions in the $TiO_2$-$TeCl_4$ systems, and large anatase single crystals could only be synthesized with the aid of Al-stabilization [22]. A special form of mesoporous alumina has been frequently used as a template for the fabrication of anatase nanotubes and nanowires [23, 24, 25, 26, 27]. Zhang and Banfield [28] reported that the anatase-to-rutile phase transformation is retarded to higher temperatures with the addition of $Al_2O_3$ to anatase $TiO_2$. This is reminiscent of the analogous behavior of zirconia in a composite with anatase [7].

Ceder et al [29] were first to report that Al-doping is beneficial for the development of cathode materials for Li-ion batteries based on $LiCoO_2$and $LiMn_2O_4$. By theoretical arguments following from first-principle calculations, as well as by their experimental verification, it was demonstrated that Al-substitution in these oxides increases the formal potential of Li-insertion, increasing the energy density of practical batteries. Wakihara et al [30] reported that Al doping increased the cyclability of spinel $Li_xAl_yMn_{2-y}O_4$cathodes. Analogously, the cycle performance and diffusion coefficient of $Li^+$ in $LiNiO_2$ was improved by Al-substitution. However, the insertion potential of Li in $Li_xAl_yNi_{1-y}O_2$was actually smaller than that of $LiNiO_2$, which contrasts with the previously reported behavior of $LiCoO_2$ [29]. For all of the above-mentioned reasons, we were motivated to study the effect of alumina on the electrochemical performance of anatase $TiO_2$, and the results of our investigation are summarized in this paper.

## Experimental

### Materials

The synthesis of Al-stabilized titania [31] followed essentially the same synthetic protocol as that of Zr-stabilized titania [7, 18]. A solution of Keggin cations $Al_{13}O_4(OH_{24})^{7+}$was prepared by dissolving 13.1338 g of $AlCl_3.6H_2O$ in 420 ml of water, and the pH was adjusted to 3.95 with concentrated ammonium hydroxide. This solution was slowly added to a solution of $(NH_4)_2Ti(OH)_2(C_3H_2O_3)_2$(Tyzor LA, DuPont) and cetyltrimethylammonium chloride (CTAC, Lonza) as described below.

For sample A, 8.27 g of Tyzor and 8.82 g of CTAC solution were combined. Then 6.62 ml of the solution of Keggin cations was diluted to 80 ml with water, and was slowly added to the Tyzor/CTAC mixture with vigorous stirring. A white precipitate formed immediately, and this was aged in a Teflon bomb at room temperature overnight, one day at 70 °C, and 2 days at 100 °C, and subsequently isolated by washing and centrifuging. The prepared material was calcined at 450 °C for 3 h.

For samples B and C, the corresponding syntheses were performed in a similar fashion to that for sample A, except, in the case of sample B, 6.82 g of Tyzor and 33.9 ml of the Keggin cations solution were used, and, in the case of sample C, 4.54 g of Tyzor and 66.18 ml of the Keggin cations solution were used.

The Ti/Al atomic ratios found by elemental analysis after calcination were 25, 11, and 6 for samples A, B, and C, respectively. A reference Al-free blank material (further abbreviated BL) was prepared by an identical synthetic protocol as for samples A–C, but without the addition of the solution of Keggin cations. Another reference Al-free material was pure anatase from Bayer (PKP09040, surface area 154 $m^2/g$).

### Characterization

Adsorption isotherms of nitrogen (Linde, purity 5.6) at 77 K were measured on a Micromeritics ASAP 2010 instrument. Before the adsorption measurement, all samples were degassed at 350 °C overnight. X-ray diffraction measurements were carried out with a Siemens D-5005 diffractometer in the Bragg-Brentano geometry using Cu Kα radiation. The lattice constants were calculated using the Eva Diffracplus v5.0 software. Micro-Raman spectra were measured using a Jobin-Yvon T64000 spectrometer equipped with an Olympus BH2 microscope. The spectra were excited in a back scattering geometry by $Ar^+$ laser (Innova 305, Coherent), $\lambda = 514.5$ nm. The laser beam was focused either to the surface of one selected grain or into its bulk. The focus length was adjusted and measured by a micrometer manipulator on the Olympus microscope.

### Preparation of electrodes

The electrodes were prepared as described in [7, 8], by using $CH_3COOH$ and Triton X-100 as dispersing agent and surfactant, respectively. The powder material was first dispersed into a paste by slow mixing with 0.1 M $CH_3COOH$ under continuous mortaring. After ~20 mins of homogenization, the slurry was mixed with Triton X-100 and further homogenized. The $SnO_2$(F) coated glass from Nippon sheet Glass, 10 Ω/square, served as a support for the electrode preparation. Scotch tape at the edge of the support defined the film thickness and left part of the support uncovered for electrical contact. The film was finally calcined for 3 h in air at 450 °C. Alternatively, a titanium grid (5×15 mm, Goodfellow) was used as the electrode support. These electrodes were prepared by dip-coating; the coated area was ~5×5 mm. The prepared electrodes were dried in

air, and finally calcined as in the case of $SnO_2$(F) electrodes. The Ti-supported electrodes usually showed better mechanical stability during electrochemical cycling, but their electrochemical performance was, in general, comparable.

### Electrochemistry

Electrochemical measurements were carried out in a one-compartment cell using an Autolab Pgstat-30 (Ecochemie) potentiostat controlled using GPES-4 software. Both the reference and auxiliary electrodes were from Li metal, so potentials are referred to the $Li/Li^+$ (1 M) reference electrode. $LiN(CF_3SO_2)_2$(Fluorad HQ 115 from 3 M) was dried at 130 °C/1 mPa. Ethylene carbonate (EC) and 1,2-dimethoxyethane (DME) were dried over a 4 Å molecular sieve (Union Carbide). The electrolyte solution, 1 M $LiN(CF_3SO_2)_2$ + EC/DME (1/1, v/v) contained 15–40 ppm $H_2O$ as determined by Karl Fischer titration (Metrohm 684 coulometer). All operations were carried out under argon in a glove box (Labstar 50, M. Braun, GmbH; the working atmosphere typically contained $<1$ ppm $H_2O$ and $<1$ ppm $O_2$). In all cyclic voltammetry experiments, the direction of the first potential sweep was (1) equilibrium potential, (2) lower vertex potential, and (3) upper vertex potential.

## Results and discussion

### Structures of the samples

Figure 1 shows the X-ray diffractograms of the Al-stabilized samples A, B and C. They can be indexed as pure anatase, without any signatures from other phases (alumina, rutile, and so on). The coherent length of the anatase nanocrystals was determined from the line broadening using the Scherrer equation (Table 1). Apparently, the size of nanocrystals decreases with increasing Al content. The lattice constants were calculated from powder diffractograms (as in Fig. 1). The *a*constant increases and the *c* constant decreases with increasing Al content, even if we refer our data to the same parameters for Al-free nanocrystalline anatase (Table 1). The contraction of the *c* axis and elongation of the *a*axis causes an overall decrease in the unit cell per formula unit ($a^2c/2$). The differences are rather small, and we should also consider the experimental error in analyzing broad X-ray diffraction peaks (Fig. 1) and the natural variations of lattice constants for various preparations even in the case of pure nanocrystalline anatase. Hence, the lattice constants may not necessarily scale with the Al-content monotonously. On the other hand, the contraction of the anatase unit cell is reminiscent of the same effect in Al-doped rutile, where the cells shrinks steadily with increasing Al-content up to ~0.8 mol% $Al_2O_3$, which is considered to be the "solubility" of $Al_2O_3$ in rutile [19].

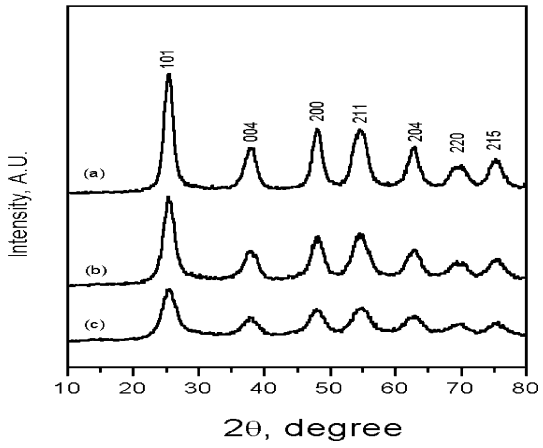


**Fig. 1** XRD patterns of samples A–C indexed as the anatase phase

The solubility of $Al_2O_3$ in anatase is unknown [19], but we may assume, from the analogy, that Al can take the form of either isomorphic (substitutional or interstitial) doping in the anatase lattice, or it can form some X-ray amorphous separate phase of ultrasmall nanocrystals ($Al_2O_3$ or $Ti_xAl_yO_2$) embedded in-between the anatase nanocrystals. The isomorphic doping by Al is also supposed for other oxidic structures [30, 32], while in the Al-$TiO_2$ system, it plays a decisive stabilizing role for the formation of macroscopic crystals (containing ~0.2% Al) [22]. Apparently, the substitution of $Ti^{4+}$ (ionic radius 0.605 Å) by $Al^{3+}$ (ionic radius 0.535 Å, octahedral O-coordination) gives rise to the compression of the unit cell and/or $TiO_6$ octahedra. The O-vacancies, which are created by isomorphic $Al^{3+}/Ti^{4+}$ substitution or interstitial doping, provide the driving force for the lattice distortion [19], and for the structural stabilization of the anatase single crystal [22].

The isomorphic substitution of Ni by Al in $LiNiO_2$ analogously enhances the structural stability [32]. On the

**Table 1** Structural and electrochemical properties of Al-doped $TiO_2$ samples, compared to those for pure anatase

| Property | Sample A | Sample B | Sample C | $TiO_2$ anatase | |
|---|---|---|---|---|---|
| | | | | Bayer[a] | BL[b] |
| Ti/Al (atomic) | 25 | 11 | 6 | ∞ | ∞ |
| $Al_2O_3$(wt%) | 2.5 | 5.5 | 9.6 | 0 | 0 |
| Crystal size (nm) | 5.6 | 4.1 | 3.0 | 10 | 21 |
| a-constant (Å) | 3.7810 | 3.8075 | 3.7875 | 3.7760 | – |
| c-constant (Å) | 9.3807 | 9.3664 | 9.3363 | 9.5139 | – |
| $S_{BET}$($cm^3$/g) | 55 | 92 | 185 | 154 | 73 |
| $V_{ME}$($cm^3$/g) | 0.036 | 0.062 | 0.110 | –[c] | –[c] |
| $D_{ME}$ (nm) | 2.6 | 2.7 | 2.4 | –[c] | –[c] |
| $E_f$ (V vs. $Li/Li^+$) | 1.85 | 1.84 | 1.83 | 1.88 | 1.85 |
| $k_0$·($10^{10}$cm/s) | 2.3 | 0.9 | 0.9 | 3.0 | 5.0 |
| $D$·($10^{17}$$cm^2$/s) | 5.4 | 6.5 | 6.0 | 3.4 | 4.6 |

$S_{BET}$ = BET surface area; $V_{ME}$ = mesopore volume; $D_{ME}$ = mean mesopore diameter; $E_f$ = formal potential of Li-insertion; $k_0$ = rate constant of Li-insertion; $D$ = chemical diffusion coefficient of $Li^+$; [a] Bayer PKP09044 (reference material of pure anatase); [b] BL = blank synthesized as A–C, but without addition of Al-precursor; [c] mesoporous ordering is not defined

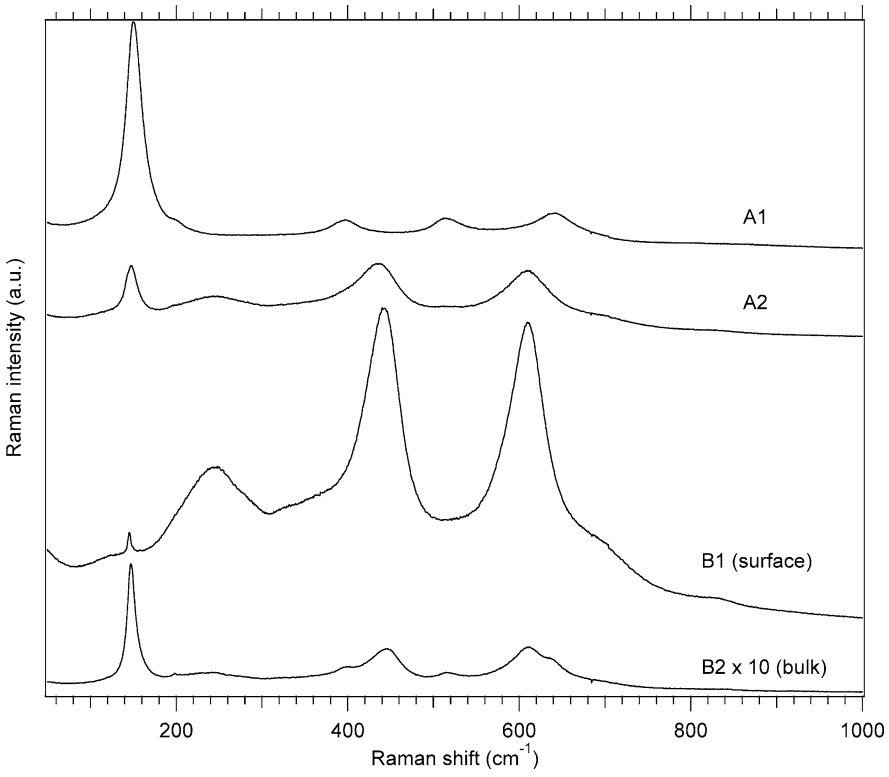


**Fig. 2** The micro-Raman spectra. A1: typical spectrum of sample A; A2: selected grain of sample A showing the rutile phase on the surface; B1: sample B with laser focus at the surface; B2: the same position of laser spot as for B1, but laser focus moved by ~2 μm into the bulk. The spectra are offset for clarity, but the intensity scales are identical for spectra A1, A2, and B1. The intensity was multiplied by a factor of 10 for the spectrum B2

other hand, bimodal morphology is assumed in zirconia-stabilized anatase [18], since the formation of solid solution of Zr in anatase is limited to low concentrations of Zr only [8]. We cannot distinguish from the present X-ray data (Fig. 1) between the isomorphic doping or bimodal structures. However, oxygen vacancies in the lattice can hardly compensate for large concentrations of Al in $TiO_2$, as for example, in sample C, and both structures need to coexist in the Al-rich materials. Assuming the $Al_2O_3$ solubility to be similar in anatase and rutile (≈0.8%) [19], all of our samples A–C are already saturated with substitutional/interstitial doping, and their structures are bimodal. From the standard Gibbs energy of formation, the $Al_2O_3$ is more stable (−1582.4 kJ mol$^{-1}$) than $TiO_2$ (−889.5 kJ mol$^{-1}$). Consequently, the strong covalent interactions Al-O-Ti, either within the lattice or at the interface of the anatase/Al-rich phase, contribute to the distortion of the anatase lattice.

Further insight into the structure and phase composition of our materials is obtained from micro-Raman spectroscopy. This technique allows a local analysis to be carried out on a sample area of ~1×1 μm$^2$. It upgrades the data from powder X-ray diffraction. The latter technique gives bulk information only, evidencing the sole presence of anatase in samples A–C (Fig. 1). The micro-Raman spectra of sample A (with the lowest content of Al) usually confirmed the presence of pure anatase. Curve A1 in Fig. 2 is a typical Raman spectrum of the sample A. Sometimes we were able to select grains of different spectra in sample A (see curve A2 in Fig. 2), which is characteristic of rutile. However, a more detailed investigation indicated that sample A was not composed of isolated grains of anatase and rutile, but that the rutile formed a surface layer on the anatase core.

This core/shell morphology is expressed more explicitly in sample B (see Fig. 2). The laser focus was moved from the surface (B1) to ~2 μm into the bulk of the material (B2). Such Raman depth profiling indicates that the surface layer is composed of rutile, whereas the bulk of the sample is formed of anatase (the spectrum B2 is actually a convolution of the surface and bulk signal, due to laser focusing). Similar behavior was also found for sample C [31]. Our data is reminiscent of the data obtained by Zhang et al [33], who have reported on the micro-Raman detection of rutile and brookite on the surface of anatase grains made by vapor hydrolysis of Ti(IV) tetraisopropoxide. Also in this case, the core/shell morphology was selectively detected by micro-Raman spectroscopy, even though the material exhibited only the anatase diffraction pattern [33].

The mechanism of rutile formation in Al-stabilized materials is unknown. We may only note that, in contrast to the materials A–C, no rutile shell was detected in the Zr-stabilized material PNNL-1, prepared by a very similar synthetic protocol [7]. All Raman spectra of PNNL-1 showed the anatase peaks independent of the laser focusing.

Nitrogen adsorption isotherms on samples A–C are shown in Fig. 3. The shapes of these isotherms are similar to those of aluminosilicate mesoporous molecular sieves with a pore size under 3 nm [34]. They are characterized by an almost linear increase in the adsorbed amount in the region of $p/p_o$ between 0.1–0.4, in

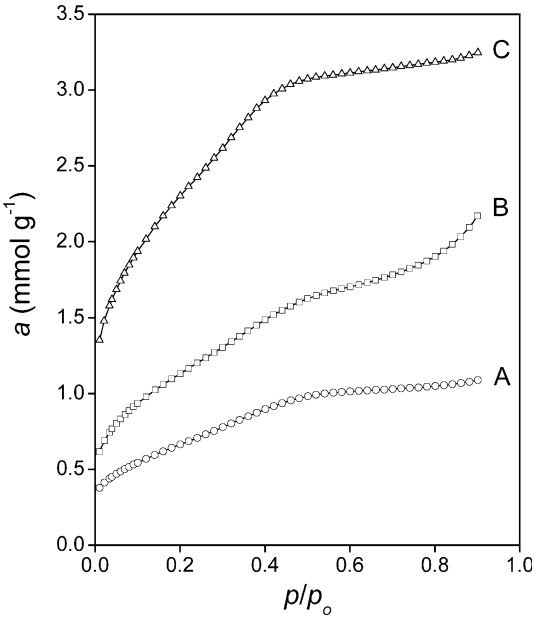


**Fig. 3** Adsorption isotherms of nitrogen at 77 K on samples A–C

which the mesopore filling occurs. A small increase in the adsorbed amount at higher relative pressures corresponds to the adsorption on the outer surface of particles. The upward deviation of the isotherm of sample B at $p/p_o > 0.7$ can be explained as a consequence of capillary condensation of nitrogen in the interparticle space.

The BET surface area, $S_{BET}$, was calculated using data in a relative pressure range from 0.05–0.20. The mesopore volume $V_{ME}$ was determined from the amount adsorbed at the relative pressure $p/p_o = 0.6$. The mesopore diameter $D_{ME}$ was calculated by means of the geometric formula $4V_{ME}/S_{BET}$. These data (Table 1) reveal that (i) the dispersity of aluminum doped $TiO_2$ is lower than that of aluminosilicate mesoporous molecular sieves, and (ii) the content of aluminum plays a decisive role. Sample A, containing formally 2.5 wt% of $Al_2O_3$, represents a dispersed material of very low mesoporosity. It seems obvious that this sample consists of unconsolidated anatase particles with a small amount of aluminum oxide in-between them. The mesopore volume is directly proportional to the content of Al (Table 1). This dependence deviates from linearity for low Al contents, which is understandable, since even pure $TiO_2$ should have some small $V_{ME}$ value. As the size of anatase particles does not change dramatically (Table 1), it is obvious that the increase in the mesoporosity is caused by the presence of Al only. It can be supposed that the mesoporous aluminum oxide particles are in an intimate contact with the particles of anatase.

## Electrochemistry

Figure 4 shows a comparative set of voltammograms for the Al-stabilized samples A–C and the Al-free sample (BL) in 1 M $LiN(CF_3SO_2)_2$ + EC/DME (1/1, v/v) at a scan rate of 0.5 mV/s. The accommodation of $Li^+$ in the anatase lattice is indicated by cathodic/anodic peaks at ~1.7 and 1.95 V vs. $Li/Li^+$, respectively. The peaks correspond to the insertion or extraction of lithium according to the equation:

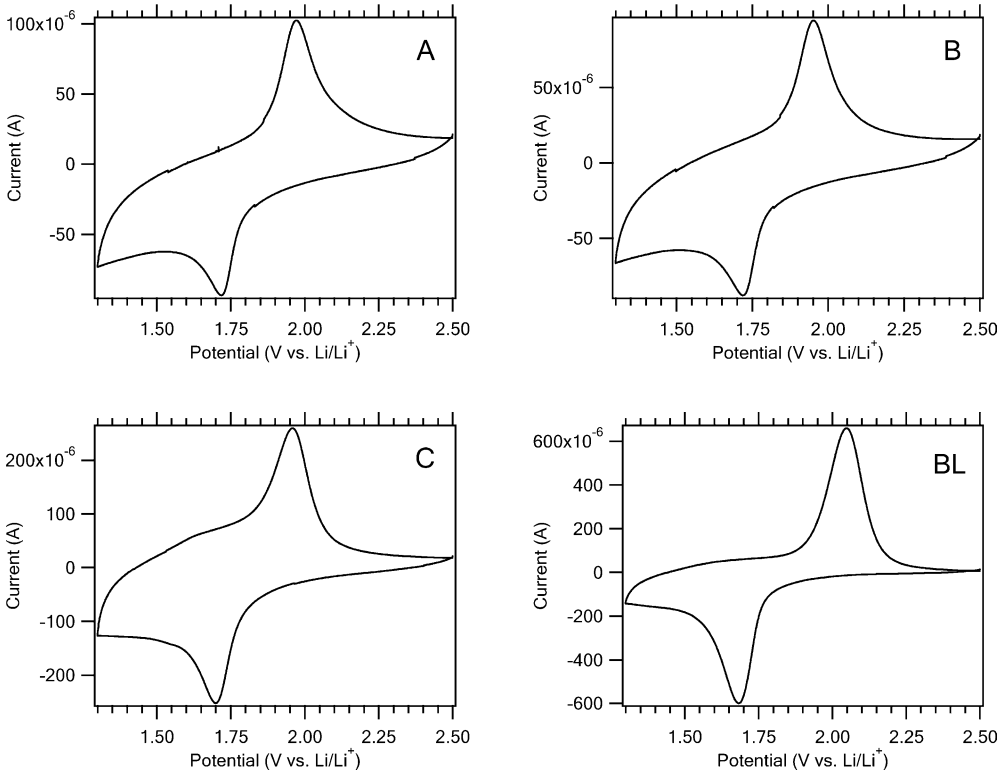


**Fig. 4** Cyclic voltammetry of Al-stabilized samples (A–C) and Al-free blank sample (BL) in 1 M $LiN(CF_3SO_2)_2$ + EC/DME (1/1, v/v); scan rate 0.5 mV/s. The mass of active electrode material is different for each of the plots shown

$$TiO_2 + x\left(Li^+ + e^-\right) \leftrightarrow Li_xTiO_2, \quad (1)$$

During the first negative voltammetric scan, electrons are injected into the Al-stabilized anatase crystal, forming $Ti^{3+}$ states, while the Al ion has a fixed oxidation state of +3. Once the process starts, $Li^+$ penetrates into the bulk material and more $Li^+$ can enter the surface until the oxide is heavily doped with $Ti^{3+}$. The Li insertion coefficient, $x$, determined from the anodic branch of cyclic voltammograms A–C, varied between 0.24 and 0.48 (somewhat smaller than that of pure anatase [7, 8, 35, 36]). Sample B usually showed the largest Li-storage capacity, close to $x = 0.5$. By comparative blank experiments, we have found that pure alumina had negligible capacity for lithium insertion. At the same conditions as for Li-insertion into anatase, the voltammetric response of alumina was dominated by capacitive charging only. Therefore, the presence of alumina may decrease the overall Li-insertion capacity of our materials. A similar drop in Li-insertion capacity was also traced for Zr-stabilized anatase PNNL-1, which, however, contained a larger proportion of the ballast inorganic component [8]. In our case, the small drop in Li-storage capacity, due to the small amounts of inactive alumina in the samples, might be compensated for by the increase in the surface area (Table 1), which promotes Li-accommodation on the voltammetric time scale. This provides a rational for the optimum performance found for sample B.

Reaction (1) was extensively studied with anatase electrodes, both theoretically [37, 38, 39] and experimentally [7, 8, 9, 22, 36, 37, 40, 41, 42, 43, 44]. These studies [43, 44, 45, 46, 47, 48, 49] demonstrated that anatase converts during reaction (1) into lithium-poor tetragonal phase $Li_{0.01}TiO_2$ with the anatase structure (space group $I4_1/amd$) and orthorhombic lithium titanate, $Li_{0.5}TiO_2$ (space group Imma). The insertion of Li into the rutile lattice is indicated by a cathodic voltammetric peak at ~1.4 V [7], which is, however, not detectable in Fig. 4. Therefore, the rutile shell (seen by Raman spectroscopy, but not by X-ray diffraction, see above) is apparently too thin to give rise to distinct voltammetric features of Li-insertion into rutile.

A more detailed analysis of the cyclic voltammograms (as in Fig. 4) shows that there is a small dependence of the formal potential of Li-insertion, $E_f$ (averaged peak potentials of the insertion and extraction processes) on the Al-content. Table 1 demonstrates that the $E_f$ values tend to decrease with increasing Al-content (from pure $TiO_2$ to sample C). This potential decrease is reminiscent of the same effect in Al-doped $LiNiO_2$ [32], but it contrasts with the opposite trend found in $LiCoO_2$ [29]. It suggests some energy barrier in Al-containing anatase, as the accommodation of Li requires more driving force (more negative potential) compared to that of pure anatase. This effect may well be due to the rutile shell on the anatase grains, since rutile is less active for Li-insertion [7, 22]. Alternatively, we may assume that the above-discussed distortion of the anatase lattice impedes the Li-insertion. If the unit cell volume decreases in Al-stabilized $TiO_2$ (vide ultra), the given amount of Li is less easily inserted into the smaller volume of the sample's unit cell compared to the more open unit cell of pure anatase. On the other hand, the increased Al-content causes a considerable increase in the BET surface area and mesopore volume (Table 1). This improves the conditions of Li-insertion, since the relative area of the electrolyte/solid interface is larger.

Another striking difference between the cyclic voltammograms of Al-stabilized materials and those of pure anatase is a broad envelope of features at potentials negative to the Li-insertion into anatase (between ~1.3–1.6 V, see Fig. 4). Voltammetric charge in this potential region indicates surface confined pseudocapacitive processes, either in amorphous titania [10] or in anatase nanosheets [11]. The observed voltammogram is also reminiscent of identical features in Zr-stabilized mesoporous anatase [7], and it is tempting to give a similar interpretation for the Al-stabilized analogues presented here.

Hagfeldt et al [36] have suggested that the cyclic voltammogram of Li-insertion into anatase can be evaluated assuming irreversible charge transfer kinetics. The standard rate constant of charge-transfer, $k_0$, can be determined from the peak current density $I_p$ and the peak potential $E_p$ according to the equation:

$$I_p = 0.227nFAck_0 \exp\left[-\alpha nF\left(E_p - E_f'\right)/RT\right], \quad (2)$$

where $n$ is the number of electrons in reaction (1), $A$ is the electrode area (approximated by its equivalent BET surface area), $F$ is the Faraday constant, $\alpha$ is the charge-transfer coefficient ($\alpha \approx 0.5$), $E_f'$ is the formal potential determined for the slowest scan (0.1 mV/s in our case), and $c$ is the maximum concentration of $Li^+$ (or $Ti^{3+}$) in the accumulation layer. Assuming the limiting composition of the insertion product to be $Li_{0.5}TiO_2$ (see reaction 1), the concentration $c$ equals 0.024 mol/cm$^3$. As the cathodic branch of cyclic voltammograms might be perturbed by parasitic breakdown reactions (like trace humidity) more accurate values can be determined for the anodic peak. The rate constant $k_0$ was calculated from several cyclic voltammograms recorded for the given electrode material at varying scan rates (between 0.1–10 mV/s). The values found (see Table 1) are greater by one order of magnitude than that of Zr-stabilized anatase of PNNL-1, $k_0 = 4.10^{-11}$ cm/s [7]. The rate constants of Al-stabilized anatase are comparable to the values of non-stabilized anatase (Table 1) as well as to those of other pure anatase nanocrystals [7, 36].

The peak current ($I_p$) also scales with the square root of the scan rate, $v$, as is expected for diffusion-controlled irreversible kinetics [36, 42]:

$$I_p = 0.4958nFAc(D\alpha nFv/RT)^{1/2} \quad (3)$$

where $D$ is the chemical diffusion coefficient of $Li^+$. Equation 3 can be used for the determination of $D$. The values found (again from the anodic branch of the cyclic voltammograms) are collected in Table 1. They compare well to the corresponding values of nanocrystalline anatase [36] and organized mesoporous anatase [10]. Generally however, the diffusion coefficients of $Li^+$ in anatase are known to vary over a broad range (from $10^{-17}$ to $10^{-13}$ $cm^2/s$) depending on the material morphology [10, 36, 42, 50]. The largest values were found for an anatase single crystal electrode $D \approx 10^{-13}$ $cm^2/s$ [22] and for compact anatase films, which were prepared by CVD or similar methods (from $10^{-15}$ to $10^{-14}$ $cm^2/s$) [41, 42, 50]. These films may mimic the single crystal electrode (for direct comparison of CVD versus nanocrystalline anatase, see [41]). In general, the diffusion coefficients tend to decrease with decreasing particle size for oxidic Li-insertion hosts [2, 3, 4]. This trend is not seen in our materials, which again illustrates the special behavior of Al-stabilized materials. Their electrochemical properties are not characterized by particle size alone; other less-common effects, such as lattice distortion and core-shell morphology, are at play. Obviously, such a complex picture should be taken into account for other Li-insertion hosts stabilized by Al and other inorganic components.

## Conclusions

Mesoporous Al-stabilized $TiO_2$ (anatase) was prepared via supramolecular templating. The material exhibited a unique core (anatase)/shell (rutile) structure, which can be seen only using micro-Raman spectroscopy, not by X-ray diffraction or Li-insertion electrochemistry.

The prepared materials exhibits a considerable increase in surface area with Al content. The mesopore volume increases in the same series, but the mesopore diameter is roughly uniform (from 2.4 to 2.6 nm).

The Li-insertion electrochemistry of our Al-stabilized materials exhibits similar features to the Zr-stabilized material, PNNL-1. In both cases, there are specific voltammetric features at potentials from ~1.3–1.6 V, which are missing in pure anatase. The Al-stabilization improves Li-insertion by enhancing the active surface area, but it also decreases the Li-storage capacity. Therefore, optimum materials are found to contain medium Al-contents.

**Acknowledgements** This work was supported by the Grant Agency of the Czech Republic through Grant No. 203/03/0824. A. Attia would like to thank the Czech Ministry of Education and Sports for partial financial support.

## References

1. Jamnik J, Maier J (2003) Phys Chem Chem Phys 5:5215
2. Levi MD, Aurbach D (1999) Electrochim Acta 45:167
3. Kavan L, Prochazka J, Spitler TM, Kalbac M, Zukalova M, Drezen T, Grätzel M (2003) J Electrochem Soc 150:A1000–A1007
4. Choi YM, Pyun SI (1997) Solid State Ionics 99:173
5. Grätzel M (2001) Nature 414:338
6. Hagfeldt A, Grätzel M (1995) Chem Rev 95:49
7. Kavan L, Attia A, Lenzmann F, Elder SH, Grätzel M (2000) J Electrochem Soc 147:2897
8. Kavan L, Grätzel M, Rathousky J, Zukal A (1996) J Electrochem Soc 143:394
9. Huang SY, Kavan L, Grätzel M, Exnar I (1995) J Electrochem Soc 142:142
10. Kavan L, Rathousky J, Grätzel M, Shklover V, Zukal A (2000) J Phys Chem B 104:12012
11. Kavan L, Kalbac M, Zukalova M, Exnar I, Lorenzen V, Nesper R, Grätzel M (2004) Chem Mater 16:477
12. Putnam RL, Nakagawa N, McGrath KM, Yao N, Aksay IA, Gruner SM, Navrotsky A (1997) Chem Mater 9:2690
13. Takahashi R, Takenaka S, Sato S, Sodesawa T, Ogura K, Nakanishi K (1998) J Chem Soc Farad T 94:3161
14. Yang P, Zhao D, Margolese DI, Chmelka BF, Stucky GD (1998) Nature 396:152
15. Yang P, Zhao D, Margolese DI, Chmelka BF, Stucky GD (1999) Chem Mater 11:2813
16. Alberius PCA, Frindell KL, Hayward RC, Kramer EJ, Stucky GD, Chmelka BF (2002) Chem Mater 14:3284
17. Crepaldi EL, Soler-Illia GJAA, Grosso D, Cagnol F, Ribot F, Sanchez C (2003) J Am Chem Soc 125:9770
18. Elder SH, Gao X, Li J, Liu D, McCready DE, Windisch CF (1998) Chem Mater 10:3140
19. Gesenhues U, Rentschler T (1999) J Solid State Chem 143:210
20. Palomares E, Clifford JN, Haque SA, Lutz T, Durrant JR (2003) J Am Chem Soc 125:475
21. Zhang XT, Liu HW, Taguchi T, Meng QB, Sato O, Fujishima A (2004) Sol Energ Mat Sol C 81:197
22. Kavan L, Grätzel M, Gilbert SE, Klemenz C, Scheel HJ (1996) J Am Chem Soc 118:6716
23. Li F, Zhang L, Metzger RM (1998) Chem Mater 10:2470
24. Lin Y, Wu GS, Yuan XY, Xie T, Zhang LD (2003) J Phys–Condens Mat 15:2917
25. Matsumuoto Y, Ishikawa Y, Nishida M, Seiichiro I (2000) J Phys Chem B 104:4204
26. Michailowski A, AlMawlawi D, Cheng G, Moskovits M (2001) Chem Phys Lett 349:1
27. Zhang X, Yao B, Zhao L, LIang C, Zhang L, Mao Y (2001) J Electrochem Soc 148:G398–G400
28. Zhang H, Banfield JF (2000) J Mater Res 15:437
29. Ceder G, Chiang YM, Sadoway DR, Aydinol MK, Jang YI, Huang B (1998) Nature 392:694
30. Song D, Ikuta H, Uchida T, Wakihara M (1999) Solid State Ionics 117:151
31. Attia A, Elder SH, Jirasek R, Kavan L, Krtil P, Rathousky J, Zukal A (2001) Stud Surf Sci Catal 135:361
32. Wang GX, Zhong S, Bradhurst DH, Dou SX, Liu HK (1999) Solid State Ionics 116:271
33. Zhang YH, Chan CK, Porter JF, Guo W (1998) J Mater Res 13:2610
34. Prokesova P, Mintova S, Cejka J, Bein T (2003) Mat Sci Eng C 23:1001
35. Kavan L, Kratochvilová K, Grätzel M (1995) J Electroanal Chem 394:93
36. Lindström H, Södergen S, Solbrand A, Rensmo H, Hjelm J, Hagfeldt A, Lindquist SE (1997) J Phys Chem B 101:7717
37. Lunell S, Stashans A, Lindström H, Hagfeldt A (1997) J Am Chem Soc 119:7374
38. Mackrodt WC (1999) J Solid State Chem 142:428
39. Nuspl G, Yoshizawa K, Yamabe T (1997) J Mater Chem 7:2529
40. Hengerer R, Kavan L, Krtil P, Grätzel M (2000) J Electrochem Soc 147:1467
41. Lindström H, Södergen S, Solbrand A, Rensmo H, Hjelm J, Hagfeldt A, Lindquist SE (1997) J Phys Chem B 101:7710

42. Van de Krol R, Goossens A, Schoonman J (1999) J Phys Chem B 103:7151
43. Van de Krol R, Goossens A, Meulenkamp EA (1999) J Electrochem Soc 146:3150
44. Van de Krol R, Goossens A, Meulenkamp EA (2001) J Appl Phys 90:2235
45. Wagemaker M, Van de Krol R, Kentgens APM, Van Well AA, Mulder FM (2001) J Am Chem Soc 123:11454
46. Henningsson A, Andersson MP, Uvdal P, Siegbahn H, Sandell A (2002) Chem Phys Lett 360:85
47. Wagemaker M, Kentgens APM, Mulder FM (2002) Nature 418:397
48. Luca V, Hanley TL, Roberts NK, Howe RF (1999) Chem Mater 11:2089
49. Wagemaker M, Kearley GJ, Van Well AA, Mutka H, Mulder FM (2003) J Am Chem Soc 125:840
50. Cantao MP, Cisneros JI, Torresi RM (1994) J Phys Chem 98:4865